A theoretical framework for dynamic anticrack and supershear propagation in snow slab avalanches

Marin Siron [a,b,1], Bertil Trottet [a,1], Johan Gaume [c,d,e,*]

[a] *School of Architecture, Civil and Environmental Engineering, Swiss Federal Institute of Technology, Lausanne, Switzerland*
[b] *Ecole Normale Supérieure de Lyon, Université Claude Bernard, Lyon, France*
[c] *Institute for Geotechnical Engineering, ETH Zurich, Zurich, Switzerland*
[d] *WSL Institute for Snow and Avalanche Research SLF, Davos Dorf, Switzerland*
[e] *Climate Change, Extremes, and Natural Hazards in Alpine Regions Research Center CERC, Davos Dorf, Switzerland*

ARTICLE INFO

ABSTRACT

Snow slab avalanches release after the failure and collapse of a weak layer buried below a cohesive snow slab. The initial failure is induced by local overloading of the slab, such that the passage of a skier. This results in the propagation of a subsidence, known as a *collapse wave* or *anticrack*. The slab may eventually break and detach from the rest of the snowpack and start to slide down, provided that the slope is steep enough to enable gravity to overcome the friction at the interface between the slab and the failed weak layer.

The approach to anticracks so far has mostly focused on (i) static configurations for the bending slab while the weak layer collapses, thereby leading to analytical conditions for the onset of an anticrack because of the metastability of the snowpack, and (ii) the observation of anticrack propagation as a result of numerical simulation methods (DEM, FEM, MPM) and field experiments (PST). The only theoretical framework to date, based on a simple modelling of the bending of the slab during the weak layer collapse, led to the well-known Heierli (2005) model which suggested an explicit solution for the propagation speed in steady state. It, however, could not account for the weak layer properties, was not mathematically bounded for certain values of the physical constants involved, and could not explain the newly uncovered "supershear" transition for steep slopes.

In this paper, a new model for the stationary propagation of anticracks is set up, so as to account for the *anticrack* speed regime on the one hand, and the *supershear* regime on the other hand, the existence of which has been recently revealed and ascertained by numerical simulations. The results presented here seem consistent with most of the available data, and highlight the role that the compaction of the weak layer can play in reducing the anticrack speed. On the contrary, by storing energy upon failure and suddenly releasing it at the crack tip, the weak layer elasticity could help justify the higher speeds sometimes observed in both regimes. Finally, a more accurate model is proposed, based on the modelling of both the slab and the weak layer as Timoshenko beams; although its complexity prevents us from solving it analytically, it provides enlightening insights into the mechanical processes at work at the interface between both layers, from a strength-of-materials perspective.

This analysis is a first step towards a better understanding of the underlying mechanisms of propagation of cracks in slab avalanches, and towards more accurate avalanche size and occurrence predictions.

---

* Corresponding author.
  E-mail address: jgaume@ethz.ch (J. Gaume).
[1] Equal contribution of Marin Siron and Bertil Trottet.

1. Introduction

Contrary to *loose snow avalanches* which typically arise in homogeneous snowpacks with very little cohesion, *slab avalanches* only occur in stratified snow, since they require the collapse of a fragile, sparse sub-layer topped by a dense slab, all of which is supported by a compact snow substrate (as depicted in Fig. 1) (Ancey, 2006; Schweizer et al., 2016). If the slope is steep enough, the slab is released following the failure and collapse of the weak underlying layer, breaking into smaller pieces which then slide downwards on the substrate. Because of the extent of the released zone, slab avalanches carry much larger volumes of snow away; thus, from a theoretical standpoint, the in-depth study of their release and flow has received increasing attention in the past decades.

The triggering mechanism of slab avalanches is now well documented. When a sufficient concentrated load is applied, e.g. by a skier or in the wake of a progressive snowfall, the weak layer breaks and locally collapses (Schweizer et al., 2003). It leads to a reduction in its volume - a so-called "volumetric collapse" - whose dynamics itself is still a topic of extensive research, due to the complexity of the constitutive law of snow (Barraclough et al., 2017; Blatny et al., 2022). This compaction of the weak layer causes the overlying slab to bend, which in turn leads to a stress concentration at the edge of the still-intact portion of the weak layer. If this stress is high enough, the edges of the latter part of the weak layer also fail and collapse. This entails the widening of the depression and, as a chain reaction, leads to the self-sustained propagation of the subsidence on both sides of the initial depression (Fig. 2).

In terms of fracture mechanics, the propagation of this "collapse wave" manifests an obvious analogy with the widening of a crack at the slab-weak layer interface, although, contrarily to an opening *mode I*, surface lips press against each other, which tends to inter-penetrate the slab and the weak layer under the effect of the load. For this reason, (Fletcher and Pollard, 1981) define the notion of *anticrack*, i.e., of a crack propagating under compression, in a closing mode (-I). Thus, the concepts of fracture mechanics are applicable to the collapse process in slab avalanches, provided that the analogy is carried out thoroughly (Heierli et al., 2008). In the following, the "collapse wave" will thus be referred to as an "anticrack".

The condition for the onset of a self-sustained propagating anticrack is generally characterised by a *critical crack length a_c*, beyond which the propagation is energetically favourable. It depends on intrinsic parameters of the snowpack, such as the mechanical properties of the layers involved, the friction between them, their dimensions, etc. It can be calculated with the Griffith-Irwin criterion (Heierli et al., 2008; Rosendahl and Weißgraeber, 2020b) or with strength-of-materials methods (eq.(9) in Gaume et al. (2017)). In practice, knowledge of the critical crack length in a snowpack is conspicuously crucial for predicting the probability of triggering of an avalanche and its size. The slope angle, compared to the *crack-face* friction angle, also plays a decisive role in the triggering of an avalanche (van Herwijnen and Heierli, 2009) (Gaume et al., 2013). In both cases, the theoretical determination of these instability criteria can be based on static considerations, since the dynamics of the anticrack is only a consequence of the pre-existing instability.
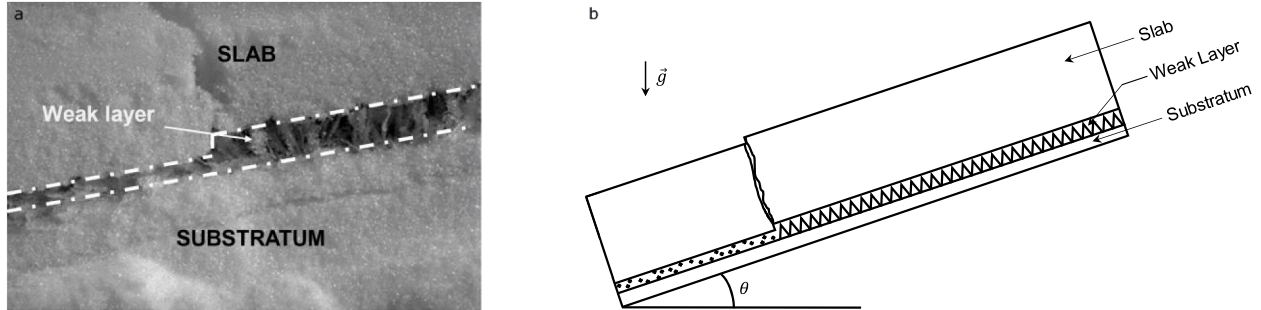

Fig. 1. Stratification of the snowpack conducive to slab avalanche initiation. (a) Well-known example of a sample stratified in three layers: the slab overlies a weak layer of partially collapsed surface hoar to the left of a central crack, and intact to the right. On the left-hand side, the partial collapse underlines the metastable aspect of this assembly in the absence of external load (gravity $\vec{g}$ excluded). The dotted lines delineate the layers (low compressible but deformable slab; compressible and deformable weak layer; substratum). © *B. Jamieson (ASARC)* (b) Schematic of the situation.
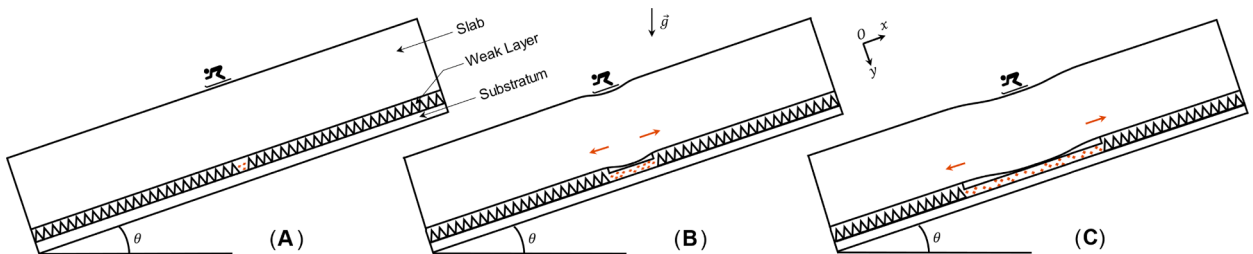

Fig. 2. Schematic of the propagation of a *collapse wave* in between a weak sub-surface layer of snow and a slab, at the onset of a snow slab avalanche, rising from birth (**A**) to a self-sustained propagating state (**C**). *Reading*: $\vec{g}$ denotes the acceleration of gravity, and (Oxy) is the frame of reference attached to the slope. The collapsed weak layer is identified by the red crosses. The arrows indicate the direction of propagation. *Note*: the diagram is not to scale. *Adapted from* (Heierli et al., 2008).

For this reason, the main theoretical investigations so far in avalanche science have focused on static collapse configurations (Benedetti et al., 2019; Gaume, Chambon, et al., 2018; Heierli et al., 2008; Rosendahl and Weißgraeber, 2020).

Recent contributions nevertheless highlight the interest of studying dynamic configurations to determine the stopping conditions of anticracks (Bergfeld et al., 2022). Besides, with the advent of numerical modelling and the increase in computational power, numerous 'numerical experiments' based on various approaches to avalanche simulation at different scales (DEM: Discrete Element Method; FEM: Finite Element Method; MPM: Material Point Method) have been made possible (Bobillier et al., 2020; Gaume, Gast, et al., 2018; Trottet et al., 2022). They have revealed several particularities specific to the dynamic behaviour of anticracks, in terms of propagation speed especially.

In particular, if a crack propagates while the slope angle is large enough, a transition takes place from a regime of *sub-Rayleigh* propagation velocities, i.e., speeds lower than that of Rayleigh waves (c_R) in the slab, to a *supershear* or *intersonic* regime, i.e., speeds between c_s and c_p (shear and dilatational plane wave velocities in the slab, respectively). The mechanism of this transition is known as that of *Burridge-Andrews* (Andrews, 1976; Burridge, 1973). It reflects a jump in the failure mechanism from a mixed mode (compressive -I and in-plane shear II) to a pure shear mode II (Trottet et al., 2022). Recently, evidence of the *sub-Rayleigh-to-supershear* transition in snow slab avalanches has been reported through avalanche video analysis. However, due to the recent nature of this evidence, researchers have not yet attempted to characterize this transition using theoretical models. As a result, currently, there is no analytical expression available that explicitly describes the velocity of the *supershear* crack in relation to the slope angle.

In the last decade, several studies have attempted to fill this gap:

- On the one hand, Heierli (2005, 2008) has laid the foundations for the dynamics of the slab in free fall, i.e. without taking into account the collapse of the weak layer that causes the slab movement. Starting from a simplistic model of a rigid plate in bending, Heierli (2005) asymptotically expresses the anticrack as the self-sustained propagation of a quasi-soliton; he proposes an explicit expression of its propagation velocity as a function of the slab parameters only, since the weak layer is not modelled. In Bobillier et al., (2021) extracted from their numerical experiments an "empirical" correction to this model, by adding terms related to the mechanical behaviour of the weak layer. The additive form of this correction, although consistent with experiments, has no physical foundation. In 2008, Heierli added complexity to the previous model by assimilating the slab to a Timoshenko beam, for which bending shear forces are added to those already taken into account. Based on an energetic approach, he derives an open system of differential equations, which couples the propagation velocity to the length of the anticrack. While the approach seems promising, it only provides an analytical expression for the velocity through costly approximations and, again, the weak layer is not accounted for.
- On the other hand, Rosendahl and Weißgraeber (2020a) sought to determine the static form of the slab in bending, by modelling both the slab (as a Timoshenko beam) and the weak layer (as a Winkler support, i.e. an elastic support in shear and compression). Their model led them to detailed criteria for the progression of the anticrack (Rosendahl and Weißgraeber, 2020b). Following energetic considerations, Heierli (2008) had also deduced an expression for the potential energy of the anticrack as a function of its distance from the origin, without attempting to introduce it into a dynamic model.

To our knowledge, however, there exists no theoretical model that simultaneously takes into account the dynamics of the slab and the contribution of the weak layer to theoretically find the collapse wave speed.

2. Outline

This study develops an analytical framework in order to characterize the dynamics of mechanical collapse waves (*anticracks*) at the interface between a weak sub-surface layer of snow and an overlying slab, during the onset of snow slab avalanches. In Section 1, we assume that an anticrack has been initiated up to the critical length a_c, beyond which propagation is self-sustained. Having passed the transient regime, the equations of motion are simplified by assuming the existence of a steady state, in order to find the asymptotic velocities and the parameters on which they depend. Section 1 details this methodology and its limits as thoroughly as possible. Section 2 establishes a general formula for the speed of the anticrack in the sub-Rayleigh configuration, and examines its behaviour for different sets of boundary conditions, drawing conclusions on the ones which are physically and mathematically acceptable. It further contains a simple model for the crack in the supershear regime. Section 3 discusses the previous expressions in light of newly available experimental and numerical data. It also expands on a more accurate modelling of the weak layer, which could account for the fracture process at the front of the anticrack, although its complexity is such that it does not seem feasible to further develop it by analytical means.

3. Methods

This section presents the methods applied to find the asymptotic propagation speed of the collapse wave in its different configurations, i.e., *sub-Rayleigh* and *supershear*. Obtaining the speed requires to solve simultaneously the equations of motion of the slab, of the weak layer and of the coupling of their dynamics through the boundary conditions. It cannot be achieved easily; thus, we decide to simplify the problem by resolving the dynamics of the slab only, and by considering the weak layer as an external resistance applied on the slab. As for the the substratum beneath the weak layer, it is assumed to be perfectly rigid in this analysis. Although the stiffness of the substratum can influence the initiation of the supershear transition, it has been demonstrated (Trottet et al., 2022) that it does not affect the steady-state crack propagation speed, which is the focal interest of the present study.
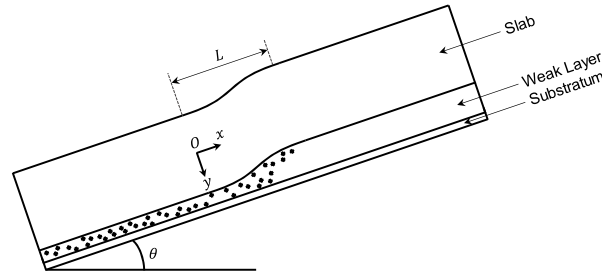
Fig. 3. Schematic of the collapse wave (anticrack) in a two-dimensional approach, valid only at large distances from the origin. The wave travels up the (Ox) axis on a slope inclined at an angle **θ** to the ground. The collapse takes place over a distance **L** such that the origin **O** of the (Ox) axis can be taken at the point of maximum compaction of the weak layer, and the point **L** corresponds to the first fracture of the still intact zone of the weak layer. The crosses mark the degraded zone of the weak layer (fracturing, compaction).

3.1. Finding the equations of motion

At first, a mechanical model of the slab has to be chosen. Following the work of Heierli (2005 and 2008) and of Rosendahl and Weißgraeber (2020a), the slab can be modelled either as a plate or as a beam, depending on the spatial extensions considered relevant.

For the sake of simplicity, in the following, we consider the slope as an infinite plane inclined by an angle θ with respect to the ground (see Fig. 3). Also, at large distances from the origin of the crack, the wave fronts become planes perpendicular to the (Ox) axis of propagation; by defining the axis reference frame as the (Oxy) plane for the collapse wave, it seems reasonable to assume invariance of the deformations in the (Oz) direction. As the problem becomes two-dimensional, the notions of plates and beams become identical. Nevertheless, it remains to choose the orientation of the propagation axis (Ox) with respect to the axis of the slope. In reality, the crack propagates in all directions from the origin of the failure, following a mixed mode (-I, II: in-plane shear, and III: out-of-plane shear) with a strong dependence on the terrain features crossed at each moment. The propagation of the anticrack is therefore different depending on whether it propagates mainly parallel or perpendicular to the slope, because the gravity components projected in the plane of the slope are distinct in these cases. In the following, the crack will be assumed to travel parallel to the slope (upwards or downwards) without loss of generality, given that any other orientation will be recoverable from our results by modifying gravity accordingly.

Modelling the slab as a so-called "Timoshenko beam" has the advantage of taking into consideration the internal shear forces in the slab; it differs from the Euler-Bernoulli beam by the absence of the traditional assumption of perpendicularity of the plane sections of the beam (or *cross sections*) to the beam generatrix (namely, the axis joining the middle of the cross sections). More comprehensive models exist (e.g., Levinson beams), yet, with the aim of facilitating the comparison of our results with the literature, we will adopt a Timoshenko beam model in the following. As for any beam model, it imposes a decoupling between the vertical and longitudinal dependencies of the displacement fields. Its kinematics assumes the following relationships for the displacement fields $u_x(x,y,t)$ and $u_y(x,y,t)$ at any point on the beam:

$$u_x(x,y,t) = u(x,t) - y \cdot \psi(x,t)$$

$$u_y(x,y,t) = v(x,t)$$

where $u(x,t)$ et $v(x,t)$ are the displacement fields in the middle of the beam sections. In steady state, the collapse wave velocity can be determined from the evolution of any point of the beam. For convenience, the generatrix of the beam is chosen, through which the velocity can be determined directly from the equations on $u(x,t)$, $v(x,t)$ and $\psi(x,t)$. Fig. 4 summarises these assumptions in a synthetic view.

In order to obtain the equations of motion of the slab, we decide to use Hamilton's Principle (or variational principle) defined from the action $\mathscr{S}$:

$$\mathscr{S}(u,v,\psi,t) = \int_t \mathscr{L}(u(x),v(x),\psi(x),t) \ dt$$

where $\mathscr{L} = \mathscr{E}_{kinetic} - \mathscr{E}_{potential}$ denotes the Lagrangian of the system and u, v, ψ are the displacement fields of the Timoshenko beam explained in Fig. 4. The principle is stated in Supplementary Material n°1.

Once this model is defined, the kinetic and cohesive energies of the beam are to be determined. Due to the scale factor of the problem (the height of the slab is very large compared to the height of the weak layer), the deformations during collapse are small, and the associated forces can be taken in their linear limit. Thus,

– Kinetic energy: $b \cdot h \cdot \int_0^L \left\{ \dfrac{1}{2}\rho\left(\dfrac{\partial u}{\partial t}\right)^2 + \dfrac{1}{2}\rho\left(\dfrac{\partial v}{\partial t}\right)^2 + \dfrac{1}{2}\rho I\left(\dfrac{\partial \psi}{\partial t}\right)^2 \right\} dx$
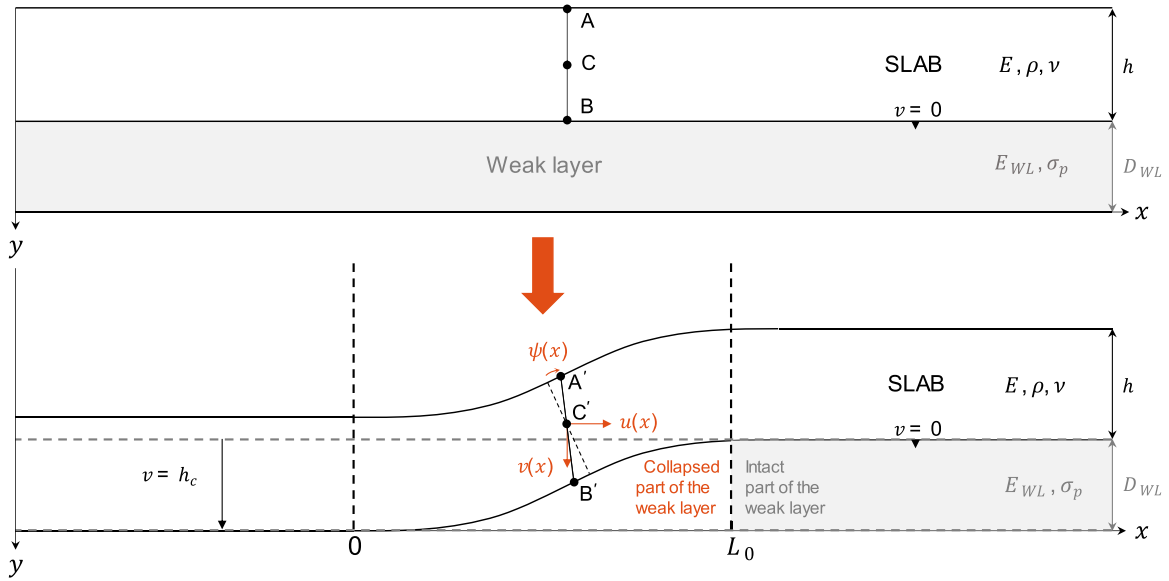
Fig. 4. Diagram of slab deformation in a Timoshenko beam model for a crack of length L_0 at time t. (Top) Intact stratified snowpack before crack initiation. (Bottom) Slab deflection after the collapse of the weak layer over a crack distance $L_0(t)$ on either side of the deflection. *Reading*: any plane section AB deformed at A'B' remains plane, but tilts by an angle ψ, with translation of its centre C by $u.\vec{x}$ and $v.\vec{y}$ to C'. The displacement fields $u(x, t)$, $v(x,t)$ and $\psi(x,t)$ depend only, in this configuration, on the longitudinal coordinate x and time t. *Note*: the diagram is not to scale.

– Tensile-compressive potential energy: $b \cdot h \cdot \int_0^L \left\{ \frac{1}{2} E \left(\frac{\partial u}{\partial x} \right)^2 \right\} dx$

– Flexural potential energy: $b \cdot h \cdot \int_0^L \left\{ \frac{1}{2} EI \left(\frac{\partial \psi}{\partial x} \right)^2 \right\} dx$

– Potential energy for shear strains: $b \cdot h \cdot \int_0^L \left\{ \frac{1}{2} \kappa G \left(\frac{\partial v}{\partial x} - \psi \right)^2 \right\} dx$. This secondary effect of flexion is specific to the Timoshenko beam theory.

with the following notations:

– $[0, L]$ defines the bending section (the part where the weak layer collapses);
– $A = b \cdot h$ is the surface of a cross section of the beam, with: h, the height of the beam/slab; b, the width of the beam.
– $I = \frac{h^2}{12}$, second moment of area of the undeformed beam (rotational moment with respect to the (Oy) axis), normalised by the surface $A = b \cdot h$;
– $E = \frac{E'}{1-\nu^2}$, plane strain Young's modulus of the beam (linked to Young's modulus E'); G, plane strain shear modulus of the beam ($G = \frac{E}{2(1+\nu)} = \frac{E'}{2(1+\nu)(1-\nu^2)}$);
– κ, called the Timoshenko correction factor, is equal to 5/6 for a rectangular beam.

Since the beam model allows us to neglect the dependency of the crack on the (Oz) dimension, *for convenience we will choose $b = 1$ throughout the rest of the paper*, without loss of generality.

Finally, one should add to these energies those of the external forces applied to the beam. This obviously includes gravity, but also contributions from the underlying weak layer, in particular the fracture energy required to fracture the weak layer during crack propagation. The modelling of this contribution is the subject of the following section.

3.2. Modelling the weak layer

The objective of this section is to establish an analytical expression for the asymptotic propagation velocities of the anticrack. To do so, the perturbation is followed at a great distance from its origin, and is assumed to have reached a stationary regime of propagation along increasing x. In a Galilean reference frame attached to the ground, each point of the perturbation is in uniform translation along the (Ox) axis at the speed c. In the mobile reference frame of axis $(0x')$ linked to the disturbance, the beam appears as static, and the
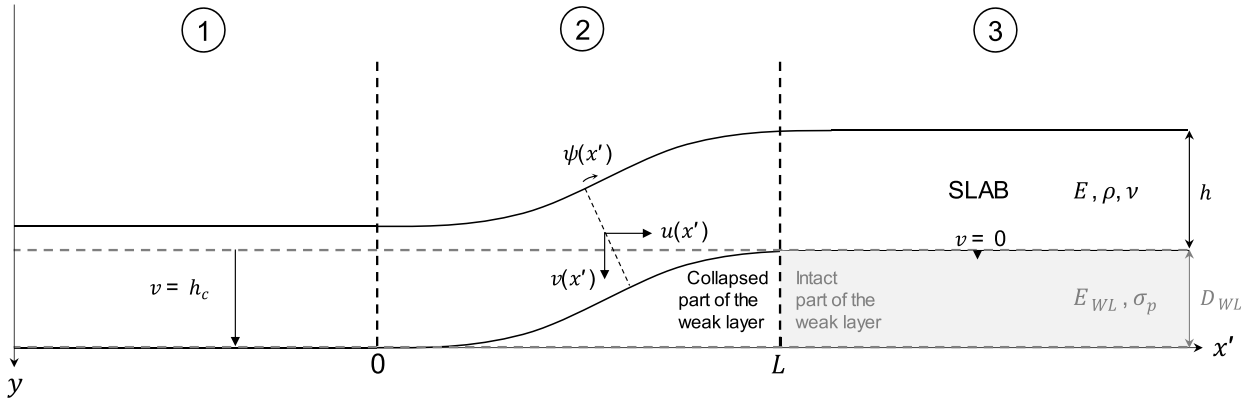
Fig. 5. Schematic of the steady state disturbance in the moving reference frame attached to the collapse wave moving from left to right at constant speed. The slab (a Timoshenko beam) can be divided into three sections. From right to left: (*Section 3*) From $+\infty$ to $x' = L$, the beam is supported by the still intact weak layer. At $x' = L$, the weak layer is suddenly fractured due to stress accumulation. (*Section 2*) From $x' = L$ to $x' = 0$, the fractured weak layer is collapsing under the weight of the overlying slab (*volumetric collapse*). The slab bends accordingly until $x' = 0$, defined as the point of tangency where it rests on the substrate after having completely compacted the weak layer. (*Section 1*) From $x' = 0$ to $-\infty$, the disturbance has passed and the weak layer has been completely compacted. The beam rests uniformly on the substrate. *Note*: the diagram is not to scale.

disturbance occupies a fixed section $]0, L[$ in this reference frame, where $L = L_0 - ct$. Fig. 5 shows the situation in this moving frame of reference.

In the end, the problem is a combination of the solutions obtained on the three sections considered separately.

3.2.1. Complete formulation of the problem

Without taking into account the work of the fracturing forces applied by the weak layer on the slab, the evolution of the displacement fields of the slab takes the following form (Heierli, 2008). On the bending section $[0, L_0(t)]$ where the collapse happens:

– *Action* functional:

$$S(u, v, t) = h \int_0^t \int_0^L \left\{ \frac{1}{2}\rho\left(\frac{\partial u}{\partial t}\right)^2 + \frac{1}{2}\rho\left(\frac{\partial v}{\partial t}\right)^2 + \frac{1}{2}\rho I\left(\frac{\partial \psi}{\partial t}\right)^2 - \frac{1}{2}E\left(\frac{\partial u}{\partial x}\right)^2 - \frac{1}{2}E\left(\frac{\partial v}{\partial x}\right)^2 - \frac{1}{2}\kappa G\left(\frac{\partial v}{\partial x} - \psi\right)^2 + \frac{\tau}{h}u - \frac{\sigma}{h}v \right\} dx\, dt$$

with $\sigma = -\rho g h \cdot \cos(\theta)$ the (negative) compressive stress due to the beam's own weight, and $\tau = \rho g h \cdot \sin(\theta)$ the shear stress due to the weight of the beam; one recalls that b has been omitted by being taken equal to 1. Continuity conditions *for the connection to the other sections*:

At time t (time dependency of the variables is therefore omitted in the following, for easier writing),
• *Continuity* of the displacement fields at $x = 0$ and $x = L_0$:

$u(0^-) = u(0^+)$	$u(L_0^-) = u(L_0^+)$
$v(0^-) = v(0^+)$	$v(L_0^-) = v(L_0^+)$
$\psi(0^-) = \psi(0^+)$	$\psi(L_0^-) = \psi(L_0^+)$

Continuity of the constraints at $x = 0$ and $x = L_0$:

Using the above-mentioned kinematics, the forces of the Timoshenko beam for low deformations are defined by:

• The bending moment $\mathcal{M} = -EAI\psi'(x, t)$
• • The transverse shear force $\mathcal{Q} = \kappa GA \cdot (v'(x, t) - \psi(x, t))$
• • The longitudinal elastic force $\mathcal{N} = EAu'(x, t)$

Their continuity at the edges implies that of $v' - \psi$, u', ψ' and, by making use of the continuity of the displacement fields, that of v', u', ψ' as well:

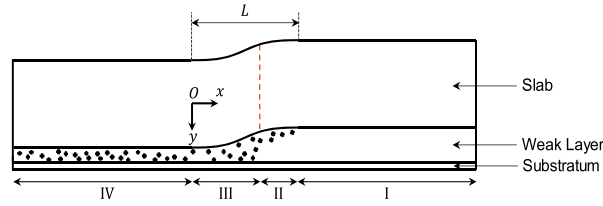|	
$u'(0^-) = u'(0^+)$	$u'(L_0^-) = u'(L_0^+)$
$v'(0^-) = v'(0^+)$	$v'(L_0^-) = v'(L_0^+)$
$\psi'(0^-) = \psi'(0^+)$	$\psi'(L_0^-) = \psi'(L_0^+)$

Fig. 6. Schematic representation of a propagating *anticrack* on flat terrain far from its origin. *Reading*: "The crack tip propagates from left to right. In region I, weak-layer bonds are not yet fractured, while in region IV all weak-layer bonds are broken. Region II is the fracture process zone, extending from the first bond fractures to the crack tip. In region III, the slab further subsides causing the weak-layer structure to fracture multiple times before closer packing of the weak layer is achieved and the slab comes to rest again." The orange dotted line refers to the position of the crack tip, while black marks denote broken bonds; L is the touch-down distance. © *Adapted from* (Bergfeld et al., 2022), *with its original legend.*

- *Boundary conditions for stresses*: in addition to the guaranteed continuity of constraints at the edges, the value of these *constraints* can be specified using the variational principle. Free edges, for instance, require vanishing moments and internal forces, leading to $v' = \psi' = u' = 0$ in such cases.

The previous equations and conditions can then be simplified by using the moving frame of reference, which results in the removal of the time dependence and in the substitution of $L_0(t)$ by L.

3.2.2. Adding a fracture force

The modelling of the fracturing process, that must be incorporated into the equations of motion, is the main novelty of this study. As the equations are derived from an energy reasoning, we seek a local expression for the energy dissipated during snow fracturing as the anticrack propagates.

The physical processes involved during brittle layer failure have recently been summarised by Bergfeld et al. (2022), whose comprehensive explanatory diagram is adapted in Fig. 6. Note that this description is only valid in the sub-Rayleigh propagation regime, where the anticrack is essentially reduced to a transverse disturbance.

As a granular medium, the snow making up the weak layer consists of *load* (or *force*) *chains*, i.e. preferential paths of connected grains that channel stress in the layer under load. Bergfeld et al. (2022) highlight that the fracturing of the weak layer at the *crack tip* (or crack front) is microscopically linked to the rupture of these load chains when the disturbance passes. The arrival of the anticrack on an intact zone of the weak layer generates the first fracturing of all the pre-existing load chains: this step, which occurs at the front of the disturbance, is the first to be energy-consuming. At the end of this initial fracture, in the sub-Rayleigh regime, the debris of the weak layer are compacted by the rest of the disturbance. However, snow crystals in these debris reorganise very frequently and create new bonds between each other, which must be broken continuously to compact them: this requires an ever-renewed energy during compaction, to develop secondary cracks in these new bonds. Thus, the compaction of the weak layer takes place progressively, until it stops when the packing of the weak layer is too strong to ensure further compaction. Based on this observation, Bergfeld et al. (2022) identify two different fracturing zones, associated with two distinct sources of energy consumption:

- The *dissipation of dynamic fracture*: it accounts for the initial energy supplied to the front of the anticrack to break the initial force chains, break the bonds at the head of the crack tip, and generate local plastic deformations.
- The *dissipation of compaction*: downstream of the anticrack front, the weak layer is progressively compacted, calling for the provision of adequate energy, microscopically linked to the friction and bond-breaking during this compaction.

These two energies must now be expressed. Two different visions can be used to achieve it.

3.2.2.1. Through fracture mechanics.
One interest in having expressed the collapse of the weak layer as an anticrack (a 'compressive fracture', whose lips close rather than open, as opposed to Mode I) is the analogy it offers with the tools of fault mechanics. Indeed, it is possible to use failure criteria (e.g., the Griffith criterion) so as to specify the work required to "open" an anticrack over a length dx' in the weak layer of arbitrary thickness b:

$$W_f^{dyn} = w_f \cdot b \cdot dx'$$

By analogy, this clearly embodies the *dissipation of dynamic fracture*. In this expression, w_f therefore refers to the specific fracture energy (per unit of crack area, in $J.m^{-2}$) to be provided to remove bonds and create a $b \cdot dx'$ surface of anticrack in the weak layer. As pertains to the *dissipation of compaction*, it can be expressed in the same way:

$$W_{comp} = w_{comp} \cdot b \cdot dx'$$

Formulated in this way, however, these works are not convenient to use in our problem, as they do not explicitly depend on any displacement field of the disturbance (u, v, ψ), although it is clear that the energy dissipated by the compaction of the weak layer

increases with the collapse height of the latter. In other words, since the compaction occurs in volume and not in surface, a volumetric compaction energy is more suitable for the situation. Following the assumption made by Bergfeld et al. (2022), we can then write:

$$\delta W_{comp} = w_{comp}^{vol} \cdot b \cdot v(x) \cdot dx' \ \forall x' \leq L \tag{1}$$

Moreover, it has been shown (Rosendahl and Weißgraeber, 2020a) that the fracture process at $x' = L$ can be split into two contributions, since it occurs in *mixed-mode* (modes -I and II). Thus,

$$\delta W_f^{dyn} = w_{f,I} \cdot b \cdot dx' + w_{f,II} \cdot b \cdot dx' \ at \ x' = L \tag{2}$$

As *Region II* of Fig. 6 is narrow, it results in two quasi-point forces associated with these energies at $x' = L$ and given by:

$$\vec{f_I} = -\ w_{f,I} \cdot b \ \vec{e_x} \qquad\qquad \vec{f_{II}} = -\ w_{f,II} \cdot b \ \vec{e_y}$$

where $w_{f,I}$ and $w_{f,II}$ are specific energies of dynamic fracture ($J.m^{-2}$) for modes -I and II, respectively. Bergfeld et al. (2022) finally underline, based on PST experiments, that the specific work of compaction is typically *thirty times higher* than the specific dissipation of dynamic fracture: compaction thus seems to be the dominant dissipative process. For this reason, it will be considered that $\forall x' \leq L$,

$$\delta W_{fracture} \approx \delta W_{comp} = w_{comp}^{vol} \cdot b \cdot v(x) \cdot dx' \tag{3}$$

In summary: This model, based on fracture mechanics and relevant for the *sub-Rayleigh* regime, gives rise to the results presented in Section 2-A.

3.2.2.2. Through the strength of materials. The rheology of snow is particularly complex, and can be caught by an elastoplastic (Blatny et al., 2022; Gaume, Gast, et al., 2018) or even elastoviscoplastic behaviour (Cresseri et al., 2009). However, uni-axial compression and tensile tests of the weak layer can be used to extract a simplified constitutive law (see Fig. 7) (Grégoire Bobillier, 2022).

In the sub-Rayleigh regime, where the transverse deformations of the beam prevail, the fracturing of the weak layer can be considered to take place in compression mainly, and to be modelled as a brittle failure (green dotted curve in Fig. 7): this alternative model is derived in Supplementary Material n°4 and briefly analysed in Section 3-A.3.

In the supershear regime, where, conversely, longitudinal deformations are preponderant, we consider that the fracturing of the weak layer takes place in shear only, and that it can be modelled as a brittle failure too: this last model is developed in Supplementary Material n°3.

3.2.2.3. Combining both approaches. The two previous views are compatible as long as they are linked through the constitutive laws used in strength of materials. An example is given in Fig. 8 for a snowpack loaded in compression, which allows the volumetric energies to be expressed as areas under the constitutive law. As a first approximation, neglecting the plastic energy input by strain softening (area $z2$ in Fig. 7) leads to a brittle fracture in compression, thus

$$w_{f,\ mode\ -I}^{vol} = \frac{1}{2}\sigma_p\epsilon_p = \frac{\sigma_p^2}{2E_{WL}} \tag{4}$$

where E_{WL} is the Young's modulus of the weak layer, σ_p its peak stress at break (equal to its yield strength), ϵ_p its peak strain at break and D_{WL} its height. From this point of view, the work to be done to fracture a section of length dx' through a thickness D_{WL} is given by
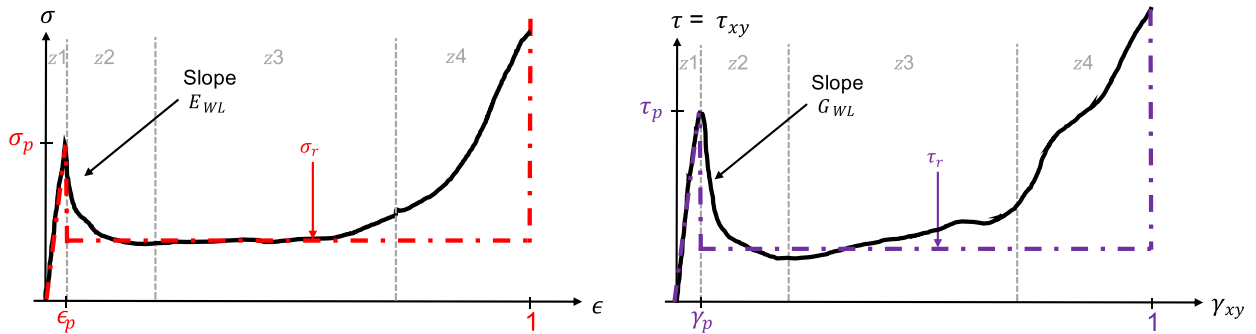

Fig. 7. (Left) Behaviour of the weak layer during a compression test under controlled load. The blue curve corresponds to the normal stress during the four phases of the collapse (elastic phase in zone $z.1$, followed by failure with softening in $z.2$; then brittle compaction in $z.3$ and densification in $z.4$). The red dotted curve corresponds to the model adopted in the *sub-Rayleigh* regime. (Right) Behaviour of the weak layer during a load-controlled shear test. The purple dotted curve now corresponds to the model adopted in the *supershear* regime, when the anticrack is in shear. *Adapted from the DEM simulations of* Bobillier (2022).

the elastic energy:

$$W_{f,\,dyn} = \frac{1}{2}\sigma_p \epsilon_p \cdot b \cdot D_{WL} \cdot dx' \tag{5}$$

whence it can be derived the specific energy of dynamic fracture:

$$w_{f,I} = \frac{1}{2}\frac{\sigma_p^2}{E_{WL}}D_{WL} \tag{6}$$

Obviously, if the fracture occurs in shear, the expression for the volume fracture energy (which has to be injected into Equation (2)) is modified according to:

$$w_{f,\,mode\,II}^{vol} = \frac{1}{2}\tau_p\gamma_p = \frac{1}{2}\frac{\tau_p^2}{G_{WL}}D_{WL} \tag{7}$$

where G_{WL} is the shear modulus of the weak layer, τ_p its peak stress at break (equal to its shear yield strength), γ_p its peak shear strain at break and D_{WL} its height.

Finally, for a mixed-mode anticrack, it can again be rewritten: $w_f^{vol} = w_{f,\,mode\,-I}^{vol} + w_{f,\,mode\,II}^{vol}$.

4. Results

In this section, we present the solutions of the problem solved with constant fracture and compaction energies, in a mixed perspective between fracture mechanics and strength of materials. The *sub-Rayleigh* and *supershear* models are treated in separate sections.

4.1. Sub-Rayleigh regime

This first model is based on fracture mechanics at speeds for which transverse strains v prevail over longitudinal strains u ($c < c_s$). As the compressive mode (-I) is predominant, we assume that the speed of the anticrack is driven by that of a flexural wave propagating in the slab, while the latter undergoes only one constant contribution from the weak layer, namely a delocalised *work of compaction* on the entire $[0,L]$ section:

$$\delta W_{comp} = w_{comp}^{vol} \cdot b \cdot v(x) \cdot dx'$$

Now that all the forces involved in the disturbed section are known, the equation of the motion of the bending in the central section can be determined (see details in Section 2 of Supplementary Material n°2):
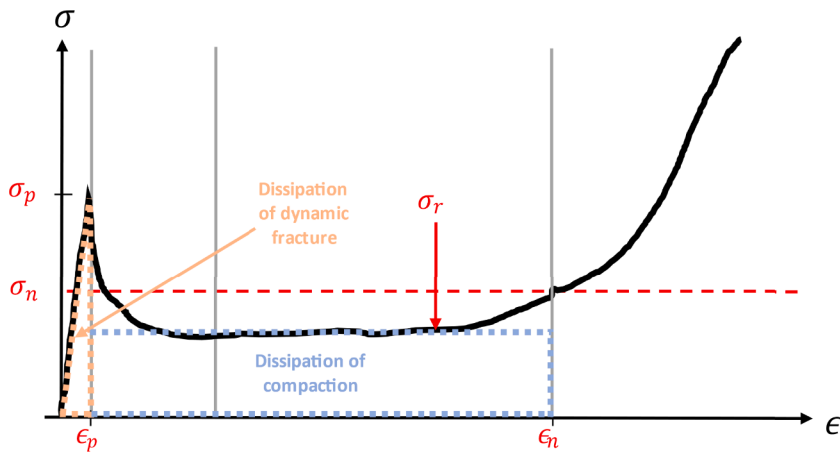

Fig. 8. Behaviour of the weak layer during a load-controlled compression test (black line), and identification of the volumetric *dissipation of compaction* and *dissipation of dynamic fracture*. When compaction occurs under realistic conditions (namely, during the collapse of the weak layer caused by the passage of an anticrack), the final stress σ_n (final strain ϵ_n, respectively) is determined by the amount of gravitational potential energy available in the slab in order to compact the weak layer. After the collapse, since the slab applies a constant stress equal to its weight when it eventually rests on the compacted weak layer, it can be inferred that $\sigma_n = \rho g h \cos(\theta)$.

$$\left(1 - \frac{c^2}{c_s^2}\right)\left(1 - \frac{c^2}{c_p^2}\right)v^{(4)} + \frac{1}{\lambda^2}\frac{c^2}{c_s^2}v^{(2)} = \frac{1}{\lambda^2 h}\Sigma_{eff} \tag{8}$$

where:

- $c_s = \sqrt{\frac{\kappa G}{\rho}}$ denotes the speed of two-dimensional shear S-waves in our Timoshenko slab;
- $c_p = \sqrt{\frac{E}{\rho}}$ denotes the speed of two-dimensional dilatational P-waves in the slab;
- $\lambda = \sqrt{\frac{EI}{\kappa G}}$ is a characteristic wavelength of the disturbance;
- $\Sigma_{eff} = \frac{\rho g h \cos(\theta) - w_{comp}^{vol}}{\kappa G}$ is the normalised effective gravity stress.

The problem must be closed by a set of boundary conditions. Six are required to close the dynamic problem, and only five for the static problem (see Supplementary Material n°6 for further details). The choice of their values is crucial, since it completely determines the velocities that can be reached.

4.1.1. Generic boundary conditions

Six boundary conditions must be brought forth to account for the six unknowns on the central collapsing section (namely, the four integration constants A, B, C, D, the speed c and the touch-down distance L). To this end, we recall the conditions used by:

- Heierli (2005):

$$v(x' = 0) = h_c \qquad\qquad \frac{dv}{dx'}(x' = L) = 0$$
$$v(x' = L) = 0 \qquad\qquad \frac{d^2v}{dx'^2}(x' = 0) = 0$$
$$\frac{dv}{dx'}(x' = 0) = 0 \qquad\qquad \frac{d^2v}{dx'^2}(x' = L) = -\frac{g}{c^2}$$

- Rosendahl and Weißgraeber (2020a): Static conditions at the junction of the sections require continuity of the displacement fields and their derivatives at $x' = 0$ and $x' = L$.

In order to provide the most general results possible, we take for granted the first three conditions of Heierli (2005), and leave the last three generic so as to match Rosendahl and Weißgraeber (2020a)'s perspective:

$$v(x' = 0) = h_c \qquad\qquad \frac{1}{h}\frac{dv}{dx'}(x' = L) = V_L'$$
$$v(x' = L) = 0 \qquad\qquad \frac{d\psi}{dx'}(x' = 0) = \psi_0'$$
$$\frac{dv}{dx'}(x' = 0) = 0 \qquad\qquad \frac{d\psi}{dx'}(x' = L) = \psi_L'$$

Obtaining the velocity explicitly is lengthy and the derivations are given in Section 5 of Supplementary Material n°2. At the end of the calculations, speed appears as a function of both the system parameters and the boundary conditions, and takes the following form:

$$\frac{c_s^4}{c^4}\lambda^2\left(1 - \frac{c^2}{c_p^2}\right)\frac{\Sigma_{eff}}{h^2}\left[\gamma\tan\left(\frac{\gamma}{2}\right)\left(1 - \frac{\psi_0'}{\frac{c_s^2}{c^2}\frac{\Sigma_{eff}}{h}}\right) + \left[\frac{\gamma}{\sin(\gamma)} - 1\right]\frac{\psi_0' - \psi_L'}{\frac{c_s^2}{c^2}\frac{\Sigma_{eff}}{h}} - \frac{1}{2}\gamma^2\left(1 - \frac{c^2}{c_s^2}\right)\right] = -\frac{h_c}{h} \tag{9}$$

$$\frac{c_s^2}{c^2}\frac{\Sigma_{eff}}{h^2}\left[\gamma\left(1 - \frac{c^2}{c_s^2}\right) - 2\tan\left(\frac{\gamma}{2}\right)\right] = -\tan\left(\frac{\gamma}{2}\right)\left(\frac{\psi_0' + \psi_L'}{h}\right) + \gamma\frac{\sqrt{1 - \frac{c^2}{c_s^2}}}{\sqrt{1 - \frac{c^2}{c_p^2}}}\frac{c}{c_s}\frac{1}{\lambda}V_L' \tag{10}$$

$$L = \gamma \lambda \cdot \frac{c_s}{c} \sqrt{\left(1 - \frac{c^2}{c_s^2}\right)\left(1 - \frac{c^2}{c_p^2}\right)} \tag{11}$$

Eqs. (9) and (10) consist of coupled equations on the variables γ and c, where γ was defined for convenience and is linked to the touch-down distance L and the anticrack speed c. Their decoupling cannot be achieved through analytical means, due to the generic boundary conditions and the equations' non-linearity; yet; their numerical resolution is straightforward and allows to find both the speed c and the touch-down distance L through the determination of γ.

The next section examines a particular case in which the analytical decoupling is made possible, leading to a generalisation of the well-known solution of Heierli (2005).

4.1.2. Generalised "Heierli Solution"

To begin with, we consider the boundary conditions (6b) and (6c) of Heierli (2005):

$$
\begin{array}{ll}
v(0) = h_c & v(L) = 0 \\
\frac{dv}{dx}(0) = 0 & \frac{dv}{dx}(L) = 0 \\
\frac{d^2v}{dx^2}(0) = 0 & \frac{d^2v}{dx^2}(L) = \frac{g}{c^2}
\end{array}
$$

Injecting them into Eqs. (9) and (10) results in Eqs. (12) to (14) below.

$$c = c_s \sqrt[4]{\frac{1}{2}\frac{E}{12(\kappa G)^2}\frac{h}{h_c}\left(\rho g h \cos(\theta) - w_{comp}^{vol}\right)\left(1 - \frac{c^2}{c_p^2}\right)\left(1 - \frac{c^2}{c_s^2}\right)} \tag{12}$$

$$L = \gamma \cdot \lambda \cdot \frac{c}{c_s}\sqrt{\left(1 - \frac{c^2}{c_s^2}\right)\left(1 - \frac{c^2}{c_p^2}\right)} \tag{13}$$

$$\gamma = \tan\left(\frac{\gamma}{2}\right) \approx 2.3311 \tag{14}$$

Let us recall the formulas for bending length L and velocity c found by Heierli (2005) (Eq. 7a) and updated in our notation system:

$$c^4 = \frac{g}{2h_c}\frac{Eh^2}{12\rho} \tag{15}$$

$$L^4 = 2.331^4\frac{2h_c}{g}\frac{Eh^2}{12\rho} \tag{16}$$

This set of equations will be referred to as the *Heierli solution* in the rest of the paper, while our equations (12) to (14) will be called the *Generalised Heierli solution*.

Several remarks can be made:

– Eq. (12) is a bi-squared fourth-order polynomial in the anticrack speed c, which means that it is theoretically possible to express its roots, although it is cumbersome, thus not detailed here for clarity. Only one positive root is expected in between 0 and c_s (as numerically ascertained).

– We recover the *Heierli solution* by considering the low-speed limit ($c \ll c_s$), no compaction process ($w_{comp}^{vol} = 0$) and a flat terrain ($\theta = 0$) in the above set of equations. It should be understood here that the equation provided by Heierli (2005) is only valid for low speeds, although no data on its range of validity was provided by the author. Please note, however, that the touch-down distance L is still different, since our Timoshenko model considers additional internal shear forces that modify the expression of λ, compared to Heierli's.

– It can be highlighted from Eq. (12) that the dissipation of compaction directly competes against gravity, so that it affects speed as though the slab was subjected to an effective gravity (smaller than *g*) during its fall; or equivalently, as though it underwent a slope angle lower than expected. The dissipation of compaction therefore appears as an *additive* term in the formula. As outlined in Section 1-B.2.c, linking the *work of compaction* (a relevant quantity for fracture mechanics) and the mechanical properties of the weak layer could contribute to give a physical basis to the additive form of the corrective terms to the *Heierli solution*, which was introduced by Bobillier (2022) for numerical simulations. Note that the dependency on the compaction process is still relatively low for classical values of $\sim 100 \ J.m^{-3}$ for the dissipation of compaction (Bergfeld et al., 2022), but significant for higher values, as displayed in Fig. 9.

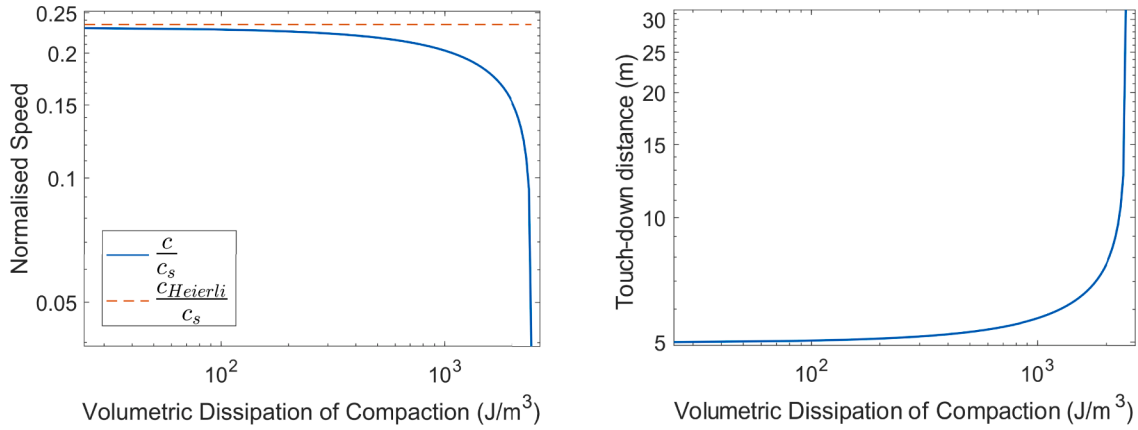**Fig. 9.** Anticrack speed c (left) and touch-down distance L (right) as a function of the volumetric dissipation of compaction. *Reading*: $c_{Heierli}$ refers to the speed out from Equation (15), c_s denotes the shear plane wave speed. *Note*: high values of compaction energy are unlikely, yet plotted to highlight the behaviour of the velocity across the entire range of effective acceleration of gravity. *Parameters*: $\rho = 250 \ kg.m^{-3}$, $E = 10 \ MPa$, $\nu = 0.3$, $b = h = 1 \ m$, $g = 9.81 \ m.s^{-2}$, $\theta = 0$.

4.2. Supershear regime

This section focuses on the *supershear* propagation regime of the crack. It is characterised by crack velocities greater than the slab shear S-waves speed c_s, and bounded by the slab compressional P-waves speed c_p.

Section 6 of Supplementary Material n°2 contains a proof that supershear speeds are inaccessible for transverse bending perturbations. Thus, when observed, the transition from a sub-Rayleigh to a supershear speed range is necessarily accompanied by a change in the mode of propagation, from a transverse to a purely longitudinal perturbation. The Burridge-Andrews mechanism justifies the transition to supershear velocities by the spontaneous nucleation, under the effect of strong tensile gravitational stress in the slab, of another crack upstream from the initial anticrack (Burridge, 1973) (Andrews, 1976). This *daughter crack* then necessarily propagates in pure shear, much faster than the initial anticrack. We thus set up a "strength-of-materials" model for this longitudinal supershear disturbance, which will convey most of the information and energy. The new situation and its parameters are presented in Fig. 10.

After the first developments in Supplementary Material n°3, postulating again the acceleration at the crack tip seems unavoidable, leading us to the following strategy: we generalise the boundary condition applied by Heierli (2005) for flexural waves, although it now involves a point force. When it exists, the latter is associated with the energy previously stored in the restoring force of the weak layer and suddenly released when the weak layer fails at the tip: provided that it is instantaneously recovered by the slab, it results in an "acceleration boost" which is expected to help increase the speed of the tip.

Starting from here, the following form for the anticrack speed is found:

$$c = \frac{c_p}{\sqrt{2}} \sqrt{\frac{\left(1 + \dfrac{\tau_b}{\tau_g - \tau_r}\right)}{\left(1 + \dfrac{1}{2}\dfrac{\tau_b}{\tau_g - \tau_r}\right)}} \tag{17}$$

where τ_b denotes the "boost stress" which can be taken equal to $\tau_p = G_{WL}\frac{u_p}{D_{WL}}$ in case of a brittle fracture (see Supplementary Material n°3 which, in addition, discusses the above assumptions).

As expected, the "boost" stress τ_b, which accounts for the restoring energy transferred from the weak layer to the slab at the tip when the fracture happens, does have the effect of increasing the velocity in the proportions defined by the previous ratio. When τ_b goes to nil, we recover a similar case to the one adopted by Heierli (2005) in the sub-Rayleigh regime, for which gravity (here reduced by friction) is the only force acting at the crack tip, leading to $c = \frac{c_p}{\sqrt{2}}$ which is the lower bound of this formula. Conversely, in the limit where τ_b grows such that $\frac{\tau_b}{\tau_g - \tau_r}$ becomes predominant over 1, $c \rightarrow c_p$, so that we recover an upper bound where the speed does not depend on any property of the two layers. Fig. 11 plots Eq. (17) as a function of the "boost stress" τ_b.

Note that, in this model, only geometrical properties of the weak layer (namely, its height) affect the velocity: the solution is independent on the geometry of the slab. The slope angle is hidden in the slope-parallel component of the gravity stress τ_p, such that it is expected to play a minor role in the formula. Nonetheless, in the absence of "boost" restoring energies, the speed is:

– To converge towards $c_p/\sqrt{2}$;
– Independent on all parameters of the weak layer, especially on its height, and on those of the slab.
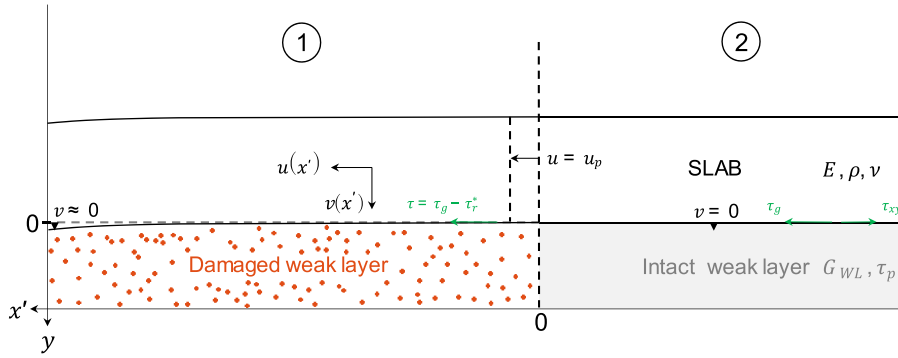
Fig. 10. Division of the slab into two sections in the moving reference frame in the *supershear* regime. (*Section 2*) From $-\infty$ to $x' = 0$, the beam is supported by the weak layer stretched elastically in shear under the effect of the slab tension due to gravity. The shear resistance is denoted τ_{xy}. At $x' = 0$, the maximum shear strain u_p is reached and the weak layer abruptly breaks. (*Section 1*) From $x' = 0$ to $+\infty$, the slab is subject, along x', only to gravity τ_g and to a constant residual friction τ_r with the debris of the damaged weak layer, lower than gravity. *Note*: the transverse displacement v and the angle ψ are neglected. Besides, the diagram is not to scale.

5. Discussion

5.1. Sub-Rayleigh regime

5.1.1. Speed adequation

The model presented here, which defines itself as an extension of the Heierli (2005) model, has the interest of alleviating the mathematical anomaly that weighed on the original formula, namely the possible divergence of the velocity according to the values given to the physical parameters. Compared to the original *Heierli solution*, the speeds that stem from our generalised model remain bounded between 0 and the limiting S-waves speed c_s, regardless of the range of physical constants involved, as shown in Fig. 12 for the collapse height of the weak layer.

The generalised solution therefore proves to be a significant improvement of the *Heierli solution*.

5.1.2. Flexural length mismatch

It can be inferred from Fig. 12 that the qualitative behaviour of the *Generalised Heierli solution* is correct as pertains to the touch-down distance: namely, the flexural length increases with the collapse height, since the free fall duration of the slab is maintained constant over the central section, whereas the height until touch-down is increasing.

However, the *Heierli solution*, and our contribution to this approach, still have a fundamental flaw related to the value given to the boundary condition on the curvature at $x' = L$. Indeed, when the speed becomes really low ($c \to 0$) or high ($c \to c_s$), the flexural length is expected to decrease (respectively, to grow) up to a *static length* L_0 (respectively, a *shear length* L_s) which stems from Equation (8) with a parameterization $c = 0$ ($c = c_s$, respectively). These conditions of junction between boundary speed values, which are stated on the
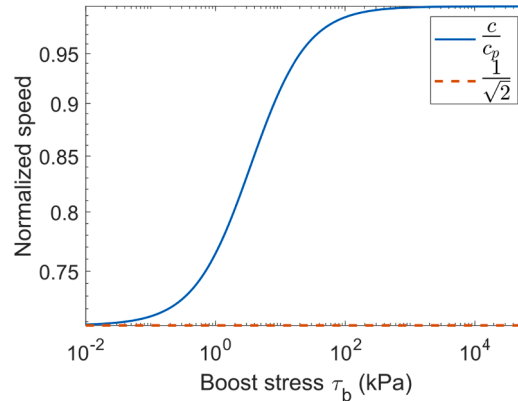

Fig. 11. Anticrack velocity as a function of the boost stress τ_b (*blue curve*), compared to the value $\frac{c_p}{\sqrt{2}}$ found without considering the fracture process of the weak layer at the crack tip (*red curve*). Parameters: $\rho = 250\ kg.m^{-3}$, $E = 3\ MPa$, $\nu = 0.3$, $g = 9.81\ m.s^{-2}$, $h = b = 1m$, $\theta = 0$.
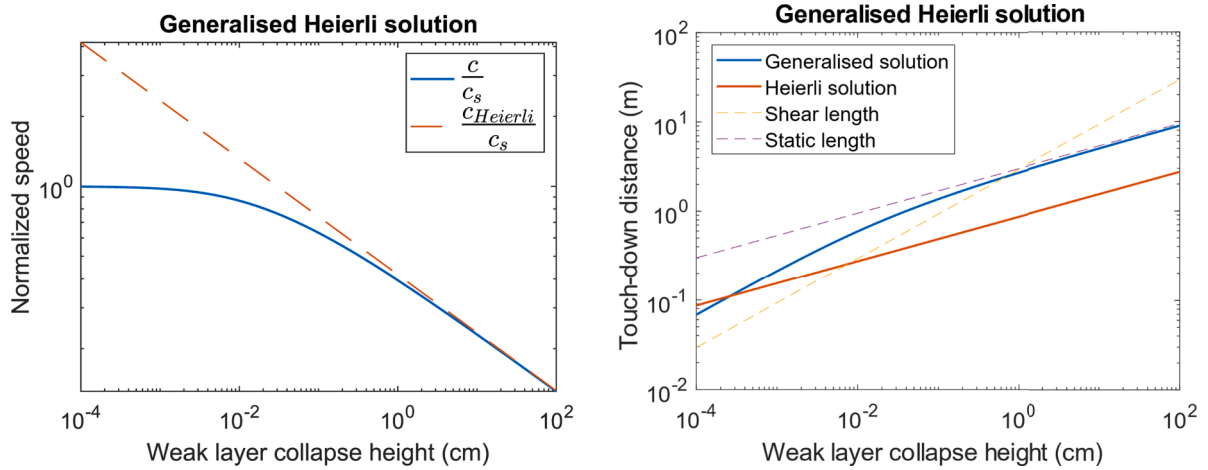
Fig. 12. (**a**) **Left**: Anticrack velocity as a function of the collapse height for our solution (*blue curve*), compared to the Heierli solution (*red curve*), in the absence of fracture energy. (**b**) **Right**: Associated touch-down distance (or *flexural length*). Parameters: $\rho = 250 \; kg.m^{-3}$, $E = 3 \; MPa$, $\nu = 0.3$, $g = 9.81 \; m.s^{-2}$, $h = b = 1m$, $\theta = 0$, $w_{comp}^{vol} = 0$.

touch-down distance L, translate into a condition on the curvature $v^{(2)}(L)$:

$$v^{(2)}(L) \underset{c \to 0}{\to} h \frac{L_0}{6} A_0' \qquad\qquad v^{(2)}(L) \underset{c \to c_s}{\to} h \lambda^2 A_0'$$

with $A_0' = \frac{\Sigma_{eff}}{(h\lambda)^2}$, $L_0 = \sqrt[4]{\frac{72 \cdot h_c \cdot h \cdot \lambda^2}{\Sigma_{eff}}}$. The complete derivation of these terms can be found as Supplementary Material n°5.

The acceleration at the crack tip *cannot be taken as a constant* with respect to the speed, and in peculiar, it cannot be the constant acceleration of gravity g that Heierli (2005) had considered. This justifies the clear mismatch in Fig. 12 (right) where the touch-down distance cannot recover its static and shear values for low and high speeds, respectively. Note that, although it is quantitatively wrong, the *Generalised Heierli solution* still shows a correct qualitative behaviour as pertains to its limiting cases, with a dependence growing as $\sqrt[4]{h_c}$ for low speeds and as $\sqrt[2]{h_c}$ for high ones; it is another enhancement to the *Heierli solution*.

Nevertheless, we found no natural form of interpolation between the two boundary values. From this point on, in the absence of knowledge on this constraint, the latter should be avoided, meaning that all velocities would remain accessible by the system. At best, a dispersion curve between a velocity and the corresponding bending length L could be given (Supplementary Material n°7):

$$L^2 = \frac{2hh_c}{\Sigma_{eff}} \frac{c^2}{c_s^2} + r^2(1 - \cos(\gamma))\left(1 - \frac{\gamma \sin(\gamma)}{1 - \cos(\gamma)} + \frac{\gamma \cos(\gamma) - \sin(\gamma)}{\gamma - \sin(\gamma)}\right) \qquad (18)$$

with $\gamma = \frac{L}{r}$ and $r = \lambda \frac{c}{c_s} \sqrt{\left(1 - \frac{c^2}{c_s^2}\right)\left(1 - \frac{c^2}{c_p^2}\right)}$. This relation still satisfies the limits:

– For $c \approx c_s$, $L \sim \sqrt{\frac{2hh_c}{\Sigma_{eff}}} \equiv L_s$
– For $c \approx 0$, $L \sim \sqrt[4]{\frac{72hh_c\lambda^2}{\Sigma_{eff}}} \equiv L_0$

5.1.3. Beyond compaction energy

Our model, which combines fracture mechanics and strength of materials, fails to provide a complete description of the phenomena involved: it requires to choose a specific value of curvature at the fracture tip *ex nihilo* - which, besides, proves to be in our case not admissible at high and low speeds. The curvature should probably not be forced, but rather obtained *via* a dynamical weak layer model, that makes use of the strength of materials to uncover a constitutive law for the still intact weak layer (Section n°3 of Fig. 5). Such a model has been put forward by Rosendahl and Weißgraeber (2020a) in a static framework, and we generalised it to a dynamic configuration in Supplementary Material n°4. In short, this model postulates that the weak layer is deformable and undergoes a brittle fracture at the anticrack tip. Although the complexity of the equations would require to solve them numerically, which is not the purpose here, it is still interesting to look at them for two reasons:

– On the one hand, the inclusion of elasticity in this model could explain the oscillations which are sometimes detected in the signals of acceleration in experiments and numerical simulations of Propagation Saw Tests (see, for instance, Figures B.5 and 3.7c in (Bobillier, 2022)).
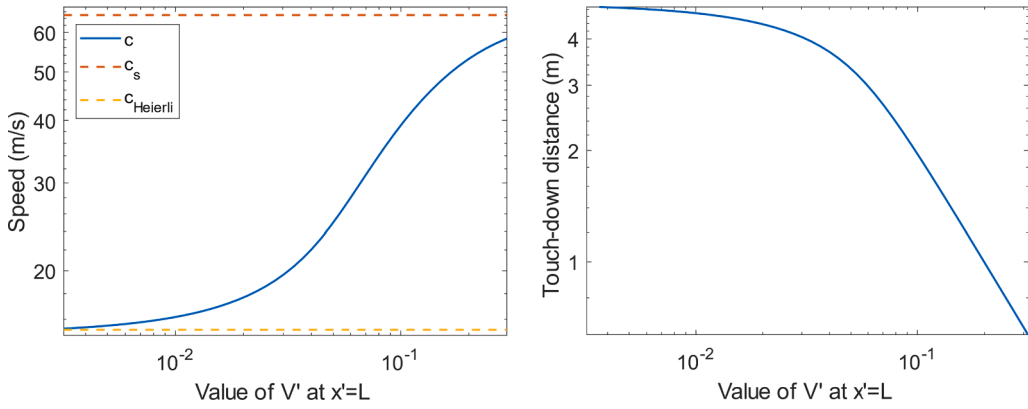
Fig. 13. (a) Left: Anticrack velocity as a function of the tangent at the crack tip (*blue curve*), compared to the Heierli solution (*yellow*) and c_s (*red*), in the absence of fracture energy. (b) Right: Associated touch-down distance. Parameters: $\rho = 250\ kg.m^{-3}$, $E = 3\ MPa$, $\nu = 0.3$, $g = 9.81\ m.s^{-2}$, $h = b = 1m$, $\theta = 0$, $w_{comp}^{vol} = 0$, $h_c = 1\ cm$.

- On the other hand, the boundary condition $v'(L) = 0$ retained until now appears to be compromised. This hypothesis meant that the slab had to horizontally tangent the weak layer at the anticrack tip. However, the model suggests that the value of the tangent is strictly positive and determined by both weak layer and slab properties. Fig. 13 plots the speed obtained by solving equations (9) and (10) for increasing values of the tangent at the crack tip. It shows that higher speeds can be recovered from this reasoning, growing from that of the *Heierli solution* up to the limit shear speed c_s. This seems more in line with the simulations when considering no fracture nor compaction (Trottet et al., 2022a).

5.2. Supershear regime

Once again, let c denote the speed of the crack in its steady state. It is not obvious at first sight whether Eq. (17) is valid or not, since there are few quantitative experimental data available as for now on the supershear transition in slab avalanches. The main numerical data set on which we rely is that of Trottet et al. (2022), derived from MPM simulations.

We recall that our theoretical model is two-dimensional, leading to characteristic velocities $c_s = \sqrt{\kappa G/\rho}$ and $c_p = \sqrt{E/\rho}$ which are built upon the *plain-strain* Young's modulus $E = \sqrt{\frac{E}{1-\nu^2}}$ instead of Young's modulus E'. Thus, to ensure comparability with the data from Trottet et al. (2022), our theoretical speed formulae must be renormalized by the three-dimensional shear wave speed $c_s^{3D} = \sqrt{\frac{G}{\rho}} = \sqrt{\frac{1-\nu^2}{\kappa}} \cdot c_s$, thereby introducing a multiplying factor $\sqrt{\frac{\kappa}{1-\nu^2}} \approx 0.96$ (with $\nu \approx 0.3$) in eq. (12) and (17).

Fig. 14 illustrates the steady-state crack propagation speed observed in MPM simulations (results from Trottet et al., 2022) as it varies with the slope angle. In this plot, two colored regions are included that represent admissible asymptotic speed values in both the *anticrack* and *supershear* regimes, based on the current theoretical analysis (Eqs. (12) and (17), respectively). The speed limits of our predictions are consistent with the outcomes of the numerical simulations.

As a further step, assuming a brittle fracture and thereby identifying the boost stress τ_b with the shear strength τ_p, it can be inferred from the simulations of supershear avalanches that $\tau_p/(\tau_g - \tau_r)$ typically varies between 1 and 12. Therefore, the range of speed values predicted in the *supershear* regime in these simulations can be refined:

$$\frac{c}{c_s^{3D}} \in [1.38; 1.68]$$

which shows a good agreement with the numerical results. Please note however that, for the *sub-Rayleigh* cases, by using the specific parameters of the simulations of Trottet et al. (2022), the theoretical admissible asymptotic speed values c/c_s^{3D} predicted by our *generalized Heierli solution* Eq. (17) are comprised within $[0.1 - 0.3]$, whereas the numerical results are rather in the range $[0.3 - 0.6]$. As raised earlier, those latter values are only recoverable by considering non-nil values of the tangent at the crack tip in the complete coupled problem of Eqs. (9) – (10). In particular, c/c_s^{3D} can grow up to 0.6 when $V'_L \sim -0.01\ m^{-1}$, which is consistent with the values arising from the temporal analysis of *anticrack* propagation (Bergfeld et al., 2022).

6. Conclusion & outlook

This paper developed a new model for dynamic anticrack propagation in slab avalanches based on the Timoshenko beam kinematics. Our speed formulas for the steady-state crack, available for both the *sub-Rayleigh* and the (newly discovered) *supershear* regime, bypass the main problems of the previously available one provided by Heierli (2005). In particular, the predicted speeds remain bounded for all values of the physical parameters involved, and consider the compaction of the weak layer derived from the
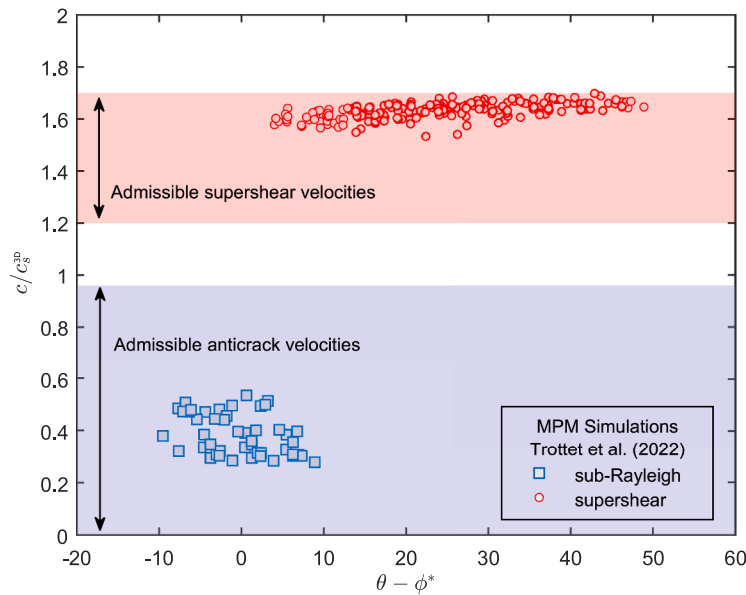
Fig. 14. Comparison between the steady-state crack speed ranges obtained based on the present theoretical analysis, and the numerical results from Trottet et al. (2022). *Reading:* on the abscissa axis, the slope angle θ is reduced by the effective friction angle ϕ^*.

perspective of fracture mechanics. For typical values of snow parameters in the slab and the weak layer, the resulting speeds show qualitatively good agreement with the available data. Quantitatively, however, they demonstrate fundamental flaws linked to the chosen boundary conditions, especially with respect to the touch-down distance for anticracks. Besides, the fracture processes at the anticrack tip were not accounted for. A more accurate model for the failure upstream from the anticrack could help explain the limitations of the present study and push the knowledge of the process a step further. Although incomplete due to the inherent mathematical difficulties encountered while deriving slightly more complex models - especially when attempting to regard fractures at the anticrack tip -, this paper underlines the robustness of our computation strategy, which could lead to an improved understanding of anticracks if more experimental data could be accessed.

The implications of this study are at least twofold: greater knowledge of the speed of an anticrack could lead not only to greater accuracy in estimating the size of avalanches when released, but also to a better estimate of the risk of their triggering. This last aspect is emphasised by Bergfeld et al. (2022) when proposing a new stability index, the *SSP* (Index for Self-Sustained Propagation), based on both static (the critical crack length) and dynamic indicators (such as the anticrack speed).

Our results do not reflect the transient dynamics of the anticrack; they especially give no information with respect to the convergence towards the steady state as a function of the weak layer parameters, on which the *supershear* regime seems to drastically depend (Trottet et al., 2022). Based on this observation, the transient dynamics of the collapse could be sought from a generalization of the expressions established by Heierli (2008) from a static perspective of the problem, whether this is achieved by (i) the differentiation of the action functional resulting from the addition of a kinetic term to the static potential of the anticrack found by Heierli (2008) in equation (4.10), or (ii) by directly searching for a dynamic potential for the anticrack following the approach that led, in the static case, to equation (4.10).

Please finally note that we have chosen to derive mixed models (involving both fracture mechanics and the strength of materials) or strength-of-materials models only. Adopting a framework utterly based on fracture mechanics could also prove to be a valuable alternative, by adapting to snow the extensive literature on transient dynamic fracture mechanics. To this end, one could draw inspiration from the works of Marder (1991) Freund (1998) and Svetlizky et al. (2017) for *anticracks*, and of Kammer et al. (2018), Bayart et al. (2018) and Shlomai et al. (2020) for the *supershear* cracks.

Author contributions

The authors contributed equally to the model, from the conception of the methodology up to the leading physical assumptions of the analytical part. M.S. performed the derivations and drafted the paper under the supervision of B.T. and J.G. J.G. defined the framework of the study and obtained the funding. All authors contributed equally to the final version of the paper.

Declaration of Competing Interest

The authors declare the following financial interests/personal relationships which may be considered as potential competing interests: Johan Gaume reports financial support was provided by Swiss National Science Foundation.

Data availability

No data was used for the research described in the article.

Acknowledgments

Supplementary materials

Supplementary material associated with this article can be found, in the online version, at doi:10.1016/j.jmps.2023.105428.

References

Ancey, C., 2006. *Dynamique des Avalanches*). Presses Polytechniques et Universitaires Romandes, Cemagref.

Andrews, D.J., 1976. Rupture velocity of plane strain shear cracks. J. Geophys. Res. 81 (32), 5679–5687. https://doi.org/10.1029/JB081i032p05679 *(1896-1977)*.

Barraclough, T.W., Blackford, J.R., Liebenstein, S., Sandfeld, S., Stratford, T.J., Weinländer, G., Zaiser, M., 2017. Propagating compaction bands in confined compression of snow. Nat. Phys. 13 (3), 272–275. https://doi.org/10.1038/nphys3966.

Bayart, E., Svetlizky, I., Fineberg, J., 2018. Rupture dynamics of heterogeneous frictional interfaces. J. Geophys. Res.: Solid Earth 123 (5), 3828–3848. https://doi.org/10.1002/2018JB015509.

Benedetti, L., Gaume, J., Fischer, J.-T., 2019. A mechanically-based model of snow slab and weak layer fracture in the Propagation Saw Test. Int. J. Solids Struct. 158, 1–20. https://doi.org/10.1016/j.ijsolstr.2017.12.033.

Bergfeld, B., van Herwijnen, A., Bobillier, G., Rosendahl, P. L., Weißgraeber, P., Adam, V., Dual, J., & Schweizer, J. (2022). *Temporal evolution of crack propagation characteristics in a weak snowpack layer: Conditions of crack arrest and sustained propagation* [Preprint]. Other Hazards (e.g., Glacial and Snow Hazards, Karst, Wildfires Hazards, and Medical Geo-Hazards). 10.5194/nhess-2022-161.

Blatny, L., Berclaz, P., Guillard, F., Einav, I., Gaume, J., 2022. Microstructural origin of propagating compaction patterns in porous media. Phys. Rev. Lett. 128 (22), 228002 https://doi.org/10.1103/PhysRevLett.128.228002.

Bobillier, G., Bergfeld, B., Capelli, A., Dual, J., Gaume, J., van Herwijnen, A., Schweizer, J., 2020. Micromechanical modeling of snow failure. Cryosphere 14 (1), 39–49. https://doi.org/10.5194/tc-14-39-2020.

Bobillier, G., Bergfeld, B., Dual, J., Gaume, J., van Herwijnen, A., Schweizer, J., 2021. Micro-mechanical insights into the dynamics of crack propagation in snow fracture experiments. Sci. Rep. 11 (1), 11711. https://doi.org/10.1038/s41598-021-90910-3.

Burridge, R., 1973. Admissible speeds for plane-strain self-similar shear cracks with friction but lacking cohesion. Geophys. J. Int. 35 (4), 439–455. https://doi.org/10.1111/j.1365-246X.1973.tb00608.x.

Cresseri, S., Genna, F., Jommi, C., 2009. Numerical integration of an elastic–viscoplastic constitutive model for dry metamorphosed snow. Int. J. Numer. Anal. Methods Geomech. https://doi.org/10.1002/nag.864 n/a-n/a.

Fletcher, R.C., Pollard, D.D., 1981. Anticrack model for pressure solution surfaces. Geology 9 (9), 419–424. https://doi.org/10.1130/0091-7613(1981)9<419:AMFPSS>2.0.CO;2.

Freund, L.B., 1998. Dynamic Fracture Mechanics. Cambridge University Press.

Gaume, J., Chambon, G., Eckert, N., Naaim, M., 2013. Influence of weak-layer heterogeneity on snow slab avalanche release : application to the evaluation of avalanche release depths. J. Glaciol. 59 (215), 423–437. https://doi.org/10.3189/2013JoG12J161.

Gaume, J., Chambon, G., Herwijnen, A.van, Schweizer, J., 2018. Stress concentrations in weak snowpack layers and conditions for slab avalanche release. Geophys. Res. Lett. 45 (16), 8363–8369. https://doi.org/10.1029/2018GL078900.

Gaume, J., Gast, T., Teran, J., van Herwijnen, A., Jiang, C., 2018. Dynamic anticrack propagation in snow. Nat. Commun. 9 (1), 3047. https://doi.org/10.1038/s41467-018-05181-w.

Gaume, J., van Herwijnen, A., Chambon, G., Wever, N., Schweizer, J., 2017. Snow fracture in relation to slab avalanche release : critical state for the onset of crack propagation. Cryosphere 11 (1), 217–228. https://doi.org/10.5194/tc-11-217-2017.

Bobillier, Grégoire, 2022. Micro-Mechanical Modeling of Dynamic Crack Propagation in Snow Slab Avalanche Release. Université Grenoble-Alpes.

Heierli, J., 2005. Solitary fracture waves in metastable snow stratifications. J. Geophys. Res. 110 (F2), F02008. https://doi.org/10.1029/2004JF000178.

Heierli, J., 2008. *Anticrack Model for Slab Avalanche Release* [PDF]. https://doi.org/10.5445/IR/1000011033.

Heierli, J., Gumbsch, P., Zaiser, M., 2008. Anticrack nucleation as triggering mechanism for snow slab avalanches. Science 321 (5886), 240–243. https://doi.org/10.1126/science.1153948.

Kammer, D.S., Svetlizky, I., Cohen, G., Fineberg, J., 2018. The equation of motion for supershear frictional rupture fronts. Sci. Adv. 4 (7), eaat5622. https://doi.org/10.1126/sciadv.aat5622.

Marder, M., 1991. New dynamical equation for cracks. Phys. Rev. Lett. 66 (19), 2484–2487. https://doi.org/10.1103/PhysRevLett.66.2484.

Rosendahl, P.L., Weißgraeber, P., 2020a. Modeling snow slab avalanches caused by weak-layer failure – Part 1 : slabs on compliant and collapsible weak layers. The Cryosphere 14 (1), 115–130. https://doi.org/10.5194/tc-14-115-2020.

Rosendahl, P.L., Weißgraeber, P., 2020b. Modeling snow slab avalanches caused by weak-layer failure – Part 2 : coupled mixed-mode criterion for skier-triggered anticracks. Cryosphere 14 (1), 131–145. https://doi.org/10.5194/tc-14-131-2020.

Schweizer, J., Bruce Jamieson, J., Schneebeli, M., 2003. Snow avalanche formation. Rev. Geophys. 41 (4) https://doi.org/10.1029/2002RG000123.

Schweizer, J., Reuter, B., van Herwijnen, A., Gaume, J., 2016. Avalanche release 101. In: International Snow Science Workshop 2016 Proceedings, Breckenridge, CO, USA, pp. 1–11.

Shlomai, H., Adda-Bedia, M., Arias, R.E., Fineberg, J., 2020. Supershear frictional ruptures along bimaterial interfaces. J. Geophys. Res.: Solid Earth (8), 125. https://doi.org/10.1029/2020JB019829.

Svetlizky, I., Kammer, D.S., Bayart, E., Cohen, G., Fineberg, J., 2017. Brittle fracture theory predicts the equation of motion of frictional rupture fronts. Phys. Rev. Lett. 118 (12), 125501 https://doi.org/10.1103/PhysRevLett.118.125501.

Trottet, B., Simenhois, R., Bobillier, G., Bergfeld, B., van Herwijnen, A., Jiang, C., Gaume, J., 2022a. Transition from sub-Rayleigh anticrack to supershear crack propagation in snow avalanches. Nat. Phys. 18 (9), 1094–1098. https://doi.org/10.1038/s41567-022-01662-4.

van Herwijnen, A., Heierli, J., 2009. Measurement of crack-face friction in collapsed weak snow layers. Geophys. Res. Lett. 36 (23), L23502. https://doi.org/10.1029/2009GL040389.